Rock Mechanics and Rock Engineering (2019) 52:1689–1703
https://doi.org/10.1007/s00603-018-1665-0

ORIGINAL PAPER

Lowest Required Surface Temperature for Thermal Spallation in Granite and Sandstone Specimens: Experiments and Simulations

Xiaodong Hu[1,2] · Xianzhi Song[1,2] · Yu Liu[1,2] · Gensheng Li[1,2] · Zhonghou Shen[1,2] · Zehao Lyu[1,2] · QingLing Liu[1,2]

Received: 7 June 2018 / Accepted: 14 November 2018 / Published online: 29 November 2018

Abstract

Thermal spallation may be economically advantageous for the drilling of deep wells and is of strong interest for the development of oil, gas and geothermal energy. The lowest required surface temperature (LRST) represents the minimal surface temperature that can induce the spallation of rock. A deeper understanding of the LRST can be used to determine when thermal spallation can be successfully initiated. However, to the best of our knowledge, comparisons of LRST in sandstone and granite have not been performed. Based on experiments and simulations, this study investigated the LRST of one type of granite and one type of sandstone in thermal spallation. First, we conducted thermal spallation experiments using rock specimens and measured the LRST by an infrared thermometer. Then, the heat flux was evaluated and compared between the sandstone and granite specimens. Meanwhile, a three-dimensional numerical model was built to simulate the heat transfer and stress distribution in the granite and sandstone specimens. The temperature and von Mises stress between the granite and sandstone specimens were compared, and then the breakage-probability factors were investigated to compare the experimental results and simulation results. This study clarifies the differences in LRST between one type of granite and one type of sandstone.

Keywords Thermal spallation · Granite · Sandstone · Surface temperature · Infrared measurements

List of Symbols

LRST	Lowest required surface temperature
A	Slope of "best-fit" line (K/s$^{1/2}$)
C	Heat capacity (J/(kg•K))
f_b	Breakage-probability factor (dimensionless)
E	Young's modulus (Pa)
F_i	Body force (Pa)
G	Shear modulus (Pa)
h_f	Heat convective coefficient [(W/(m^2 K)]
K_r	Thermal conductivity coefficient [W/(m K)]
K'	Rock expansion index (Pa)
Q	Heat flux on the rock surface (W/m^2)
Q_0	Convective heat transfer coefficient (W/m^2)
T	Temperature in the rock (K)
T_b	Temperature on the boundary (K)
T_{ext}	Temperature of ambient temperature (K)
u	Displacement (m)
α	Rock thermal diffusivity (m^2/s)
β	Thermal expansion coefficient (/K)
μ	Poisson's ratio (–)
ε_{ij}	Strain tensor (dimensionless)
ρ	Rock density (kg/m^3)
$\sigma_{ij,j}$	Stress tensor (Pa)
σ_s	Yield strength (Pa)
σ_v	Von Mises stress (Pa)
σ_1	First principal stress (Pa)
σ_2	Second principal stress (Pa)
σ_3	Third principal stress (Pa)

✉ Xianzhi Song
songxz@cup.edu.cn

[1] China University of Petroleum-Beijing, Beijing 102249, China

[2] State Key Laboratory of Petroleum Resource and Prospecting, Beijing 102249, China

1 Introduction

Thermal spallation is of strong interest for the development of oil, gas and geothermal energy. (Sierra-Pallares et al. 2009; Augustine 2009; Rothenfluh 2013; Hu et al. 2016; Song et al. 2017; Lyu et al. 2017). Compared to conventional rotary drilling technologies, thermal spallation may be economically advantageous for the drilling of deep wells (Rauenzahn and Tester 1989; Potter et al. 2010; Stacey et al.

2011; Rothenfluh et al. 2011; Hu et al. 2018a). The mechanisms of thermal spallation can be simply explained. First, when the rock surface is exposed to a hot fluid/flame jet, transferring the heat flux from the rock surface to a position far from the rock surface is difficult because of the low thermal conductivity of rock. Second, the coefficients of thermal expansion of the minerals in the rock are different. The two reasons above explain why non-uniform thermal stress is generated near the rock surface. Subsequently, pre-existing flaws near the rock surface lengthen, and then these extended flaws become connected, which causes the rock to fracture into small spalls (Preston and White 1934; Hettema et al. 1998; Augustine 2009; Walsh and Lomov 2013; Hu et al. 2018b). The lowest required surface temperature (LRST) represents the minimal surface temperature that can induce the spallation of rock, which is of significant importance in the application of thermal spallation. A deeper understanding of the LRST can help identify when thermal spallation can be successfully initiated and optimize the reaction in the chamber used to generate high-temperature fluids/flames. Since sandstone formation and granite formation are common reservoirs for oil and geothermal energy, it is necessary to clarify the LRST in sandstone and granite.

Previous investigations related to surface temperature are summarized below. Four models have been developed to evaluate the LRST. First, Carslaw and Jaeger (1959) proposed a model based on the assumption that one-dimensional, semi-infinite solids are subjected to a constant heat flux. The surface temperature is a function of the heating time required for the initiation of spallation in the surface and rock properties. Then, the LRST can be estimated when the heating time is obtained. Rauenzahn and Tester (1989) recorded a heating test on high-speed videotape and obtained the heating time and estimated the LRST in granite. Second, the surface temperature can also be estimated by a model that is a function of stand-off distance, drilling velocity and rock properties (Wilkinson and Tester 1993; Rauenzaha and; Tester 1991a, b). Third, a Weibull model has been widely used in the evaluation of surface temperature, and it is based on a function of rock properties and Weibull parameters (Dey 1984; Rauenzahn 1986; Dey and Kranz 1987; Walsh et al. 2014). Fourth, a complex numerical model different from the analytical models above was developed to simulate rock failure in the process of thermal spallation (Walsh et al. 2011; Walsh 2013; Walsh and Lomov 2013). Using this model, the damage distribution and spall features have been investigated, and the simulation result showed that the damage distribution in granite is a function of surface temperature (Walsh 2013).

The surface temperature can be measured directly by experiments featuring infrared thermometers or thermocouples. Studies have measured the surface temperature of several different granite samples heated by flame jet using an infrared thermometer (Wilkinson and Tester 1993; Brkic et al. 2015; Kant and Rohr 2016). The surface temperature of granite samples has also been measured by thermometers, and then the surface was heated by a supercritical water jet in the experiment process (Beentjes et al. 2018). All the models and experiments above were focused on granite samples, and the LRST remains to be investigated in other rock samples. Thermal spallation experiments of various rocks (granite, quartzite, rhyolite, sandstone, and limestone) were conducted, and the diameter and depth of the holes were compared after spallation (Williams et al. 1996). However, the LRST was not measured in the experiment. Based on the discussion above, a comparison of the LRST between sandstone and granite is lacking.

In this paper, we compared the LRST between one type of sandstone and one type of granite by experiment and simulation. First, we conducted the flame-jet thermal spallation experiment using one type of sandstone and one type of granite samples. We measured the surface temperature by the infrared thermometer. The LRST was obtained when the first spall appeared on the rock surface. Subsequently, we quantitatively investigated the LRST of the sandstone and granite specimen in our experiments. Furthermore, we obtained the temperature distribution and stress distribution via simulation, and the results can help to clarify the LRST of granite and sandstone used in our experiment.

2 Physical Properties of the Tested Granite and Sandstone

In this section, we measured the composition and properties of granite and sandstone samples for the experiment and simulation. Table 1 shows the composition of the granite sample and sandstone sample. The minerals in the granite sample are quartz, potassium feldspar, anorthose, dolomite, amphibole, and clay minerals, in which anorthose

Table 1 Mineral composition of the granite sample and sandstone sample

Samples	Quartz (%)	Potassium feldspar (%)	Anorthose (%)	Dolomite (%)	Amphibole (%)	Clay minerals (%)
Granite	23.2	18.2	49.8	1.2	6.6	1.0
Sandstone	83.1	0.3	4.9	–	–	11.7

occupies the largest percentage (49.8%). The minerals in the sandstone sample are quartz, potassium feldspar, anorthose and clay minerals, in which quartz occupies the largest percentage (83.1%). We measured the properties of the granite sample and sandstone samples as shown in Table 2, including the ρ, E, μ, σ_s, K_r, C which mean density, Young's modulus, Poisson's ratio, yield strength, thermal conductivity coefficient, and heat capacity. It is important to mention that the thermal expansion coefficient β for granite and sandstone is obtained from typically measured data in a previous investigation (Rauenzahn and Tester 1989). Figure 1a presents the granite sample before and after the uniaxial compression test. Figure 1b presents the stress–strain curve for granite in the uniaxial compression test. Figure 2a presents the sandstone sample before and after the uniaxial compression test. Figure 2b presents the stress–strain curve for the sandstone sample in the uniaxial compression test. The yield strength of the granite sample is larger than that of the sandstone sample. Meanwhile, the thermal conductivity coefficient in the sandstone sample is larger than that in the granite samples by 98.4%. The heat capacity in the sandstone sample is slightly larger than that in the granite sample.

3 Experimental Section

3.1 Experiment Setup

The schematic of the flame-jet thermal spallation experiment is shown in Fig. 3. A methane tank and oxygen tank provide fuel and oxygen, and the flow rates are 15 L/min and 45 L/min, respectively. Combustion is generated in the combustion chamber. The inner diameter and outer diameter of the combustion chamber are 30 mm and 56 mm, respectively. It is important to mention that combustion is initiated by an electric spark. The distance from the combustion chamber to the rock surface is 60 mm. The size of granite samples and sandstone samples are $100 \times 100 \times 100$ mm. Four holes are drilled in the rock samples to measure the temperature in the rock. The diameter and depth of holes are 4 mm and 40 mm. The distances from each hole to the rock surface are 20 mm, 40 mm, 60 mm, and 80 mm. The K thermocouples are inserted into the holes to measure the temperature. All the measured data are saved by the data collection system. An infrared thermometer is used to measure the surface temperature of the rock. The LRST is obtained when the first spall appears on the rock surface. Figure 4 shows the thermal spallation experiment using a granite sample, in which the

Table 2 Properties of the granite sample and sandstone sample

Samples	ρ (kg/m^3)	E (GPa)	μ (–)	σ_s (MPa)	K_r [W/(m K)]	C [J/(kg K)]	β (K^{-1})
Granite	2640	29.98	0.19	103.87	2.50	827.20	8×10^{-6}
Sandstone	2480	16.63	0.34	80.11	4.96	829.30	1×10^{-5}

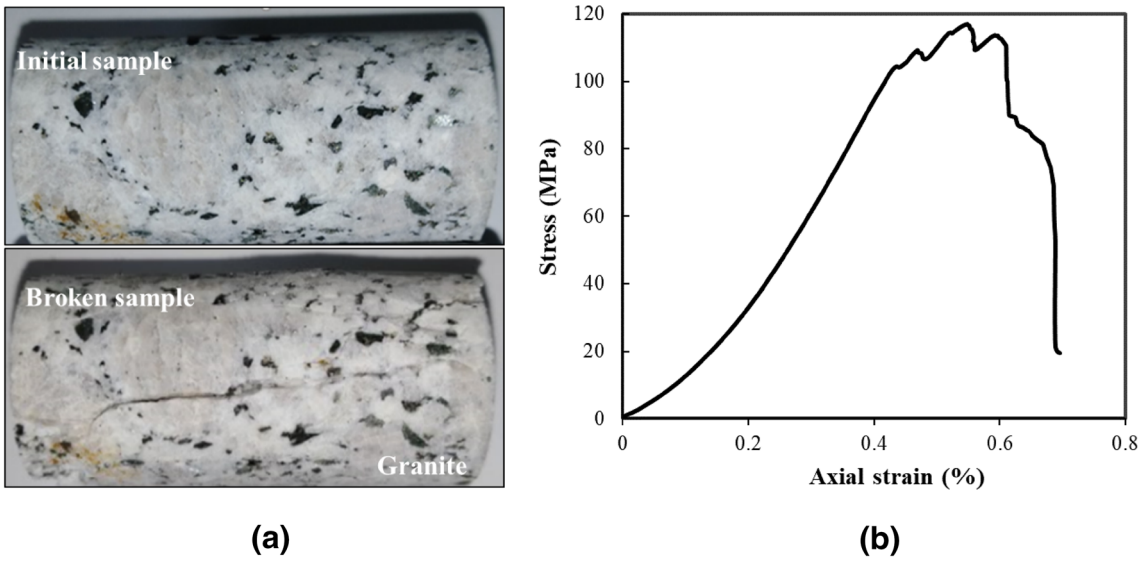

Fig. 1 Uniaxial compression test of a granite sample: **a** a granite sample before and after uniaxial compression test; **b** stress–strain curve for a granite sample in uniaxial compression test

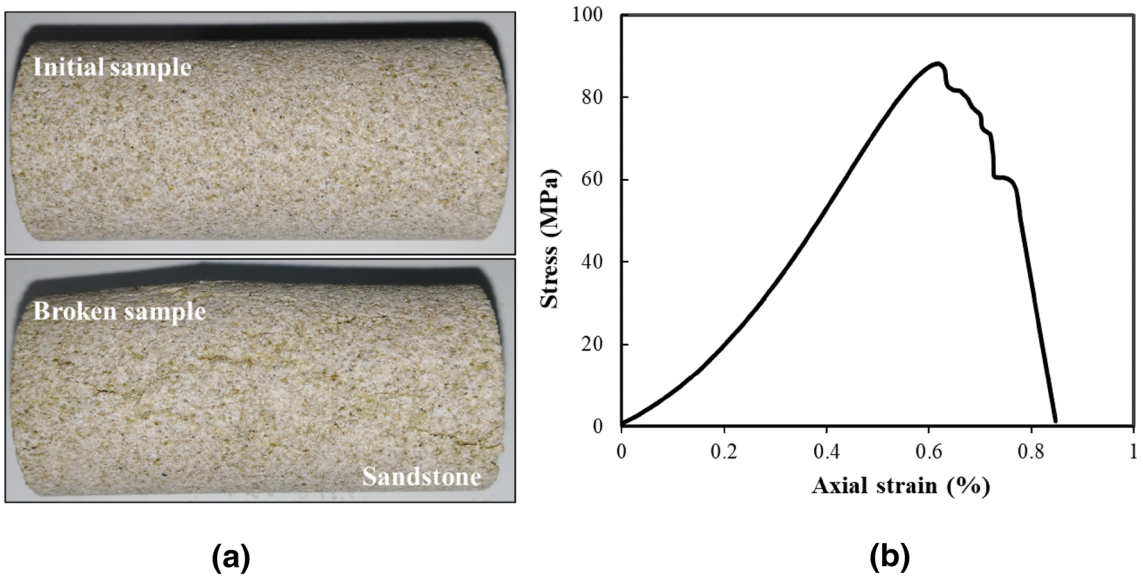

Fig. 2 Uniaxial compression test of a sandstone sample: **a** sandstone sample before and after uniaxial compression test; **b** stress–strain curve for a sandstone sample in uniaxial compression test

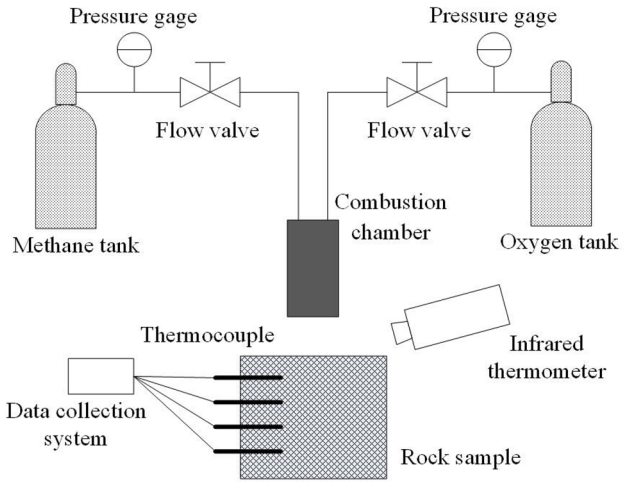

Fig. 3 Schematic of the experimental apparatus of flame-jet thermal spallation

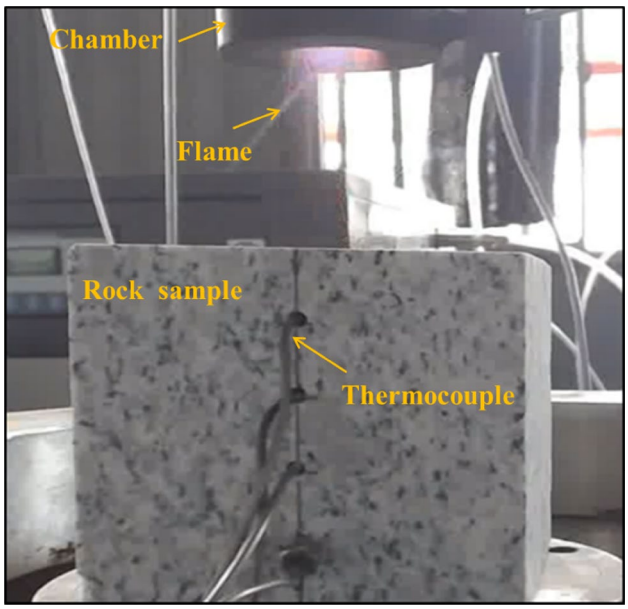

Fig. 4 Thermal spallation process using a granite sample. The combustion chamber, flame, granite sample and K thermocouple are shown in Fig. 4

reaction chamber, flame, granite sample and the K thermocouples can be observed.

3.2 Comparison of Surface Temperatures

We conducted the experiment using three granite samples and four sandstone samples. The LRST and onset-spallation time are shown in Fig. 5. The onset-spallation time means the time interval from the moment at which heating begins to the moment at which the first spall appears on the rock surface. As shown in Fig. 5a, the LRST for three granite samples are 780.15 K, 773.15 K, and 821.15 K and for four sandstone samples is 843.15 K, 893.15 K, 863.15 K and 770.15 K. The average LRST for the granite samples and sandstone samples are 791.48 K and 842.40 K, respectively. Under our experimental conditions, the average LRST in the sandstone samples is higher than that of the granite samples by 6.43%. We can infer that the type of sandstone used in our experiment is slightly harder to spall than the granite. Based

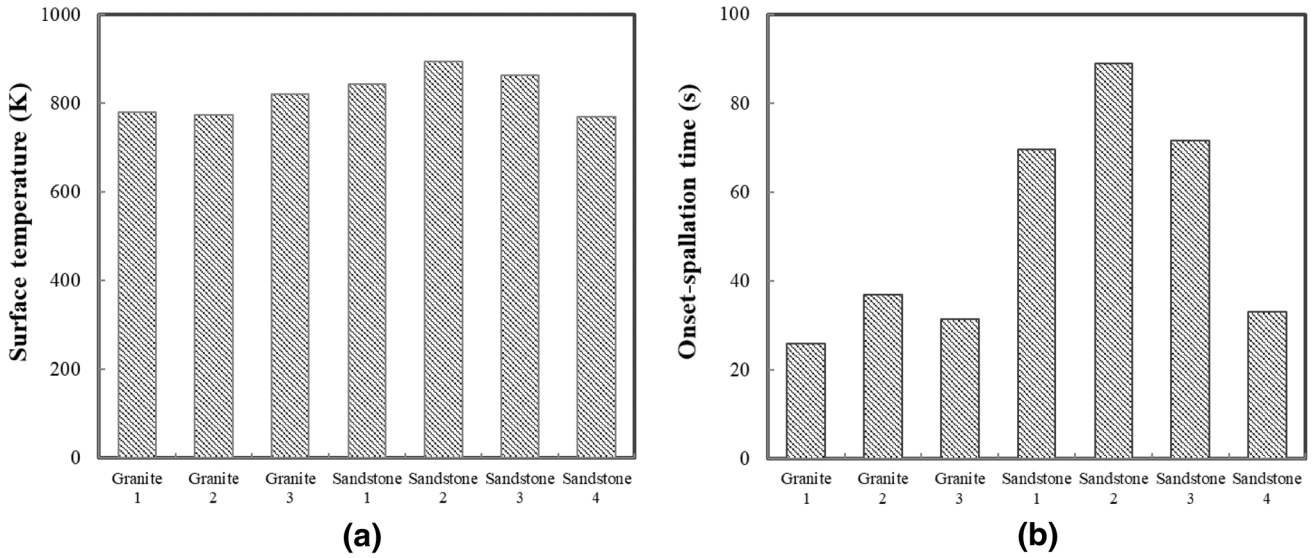

Fig. 5 Comparison of lowest required surface temperatures and onset-spallation times between granite and sandstone: **a** lowest required surface temperatures; **b** onset-spallation times

on the Weibull model in the previous investigation (Hu et al. 2018b; Walsh et al. 2014), the LRST decreases as Young's modulus increases. As shown in Table 2, Young's modulus of the tested granite specimen is higher than that of the sandstone specimen, which leads to a lower LRST in granite.

Figure 5b shows the onset-spallation time for the rock samples, which are 26, 37, and 31.5 s for the granite samples and 69.5, 89, 71.5 and 33 s for the sandstone samples. The average onset-spallation times of granite samples and sandstone samples are 31.5 s and 65.75 s, respectively. The average onset-spallation time of sandstone is longer than that of granite by 108.73%, because the pores in the sandstone may extend and connect into a micro-fracture when the surface is heated. The thermal stress can be relieved with the extension of the micro-fracture, which results in higher LRSTs and more onset-spallation time in the sandstone samples. Since the onset-spallation time of sandstone 4 is dramatically lower than that of sandstone 1, sandstone 2 and sandstone 3. Some potential error may exist in the heating experiment of sandstone 4. It is important to mention that we just use the sandstone 1, sandstone 2 and sandstone 3 for further analysis below.

3.3 Relationship Between Heat Flux and Surface Temperature

The surface temperature changes as the heat flux increases (Wilkinson and Tester 1993; Kant and Rohr 2016). An investigation of the relationship between the heat flux and surface temperature can provide a critical guideline for combustion design in thermal spallation. The heat flux can be evaluated by Eq. (1) (Carslaw and Jaeger 1959; Wilkinson and Tester 1993)

$$Q = \frac{AK_{\mathrm{r}}}{2(\alpha/\pi)^{1/2}}, \tag{1}$$

where Q is heat flux on the rock surface (W/m^2); α is the rock thermal diffusivity (m^2/s); and A is the slope of the "best-fit" line (K/s$^{1/2}$), which is obtained by linear fitting between the surface temperature and square root of heating time. The thermal diffusivity can be expressed as

$$\alpha = \frac{K_{\mathrm{r}}}{\rho C}. \tag{2}$$

To obtain the heat flux, we present the profile of the measured surface temperature with changes in the square root of the heating time as shown in Fig. 6. After that, the linear fitting is used to calculate the slope. The slopes for granite 1, granite 2, granite 3, sandstone 1, sandstone 2, sandstone 3 are 32.75, 35.76, 39.21, 17.93, 29.94, and 26.36 K/s$^{1/2}$, respectively. Based on Eq. (1), the heat fluxes corresponding to the LRST of granite 1, granite 2, granite 3, sandstone 1, sandstone 2, sandstone 3 are 6.78×10^4, 7.40×10^4, 8.12×10^4, 5.07×10^4, 8.47×10^4, and 7.46×10^4 W/m^2, respectively. Figure 7 shows the LRST profiles with changes in the heat flux. The red line represents the linear trend line fitted by the least square method. The LRST roughly increases as the heat flux increases, which has also been observed in granite samples in previous investigations (Wilkinson and Tester 1993; Kant and Rohr 2016). It is important to mention that the heat flux in this paper is smaller than that in previous investigations for two reasons (Wilkinson and Tester 1993; Kant and Rohr

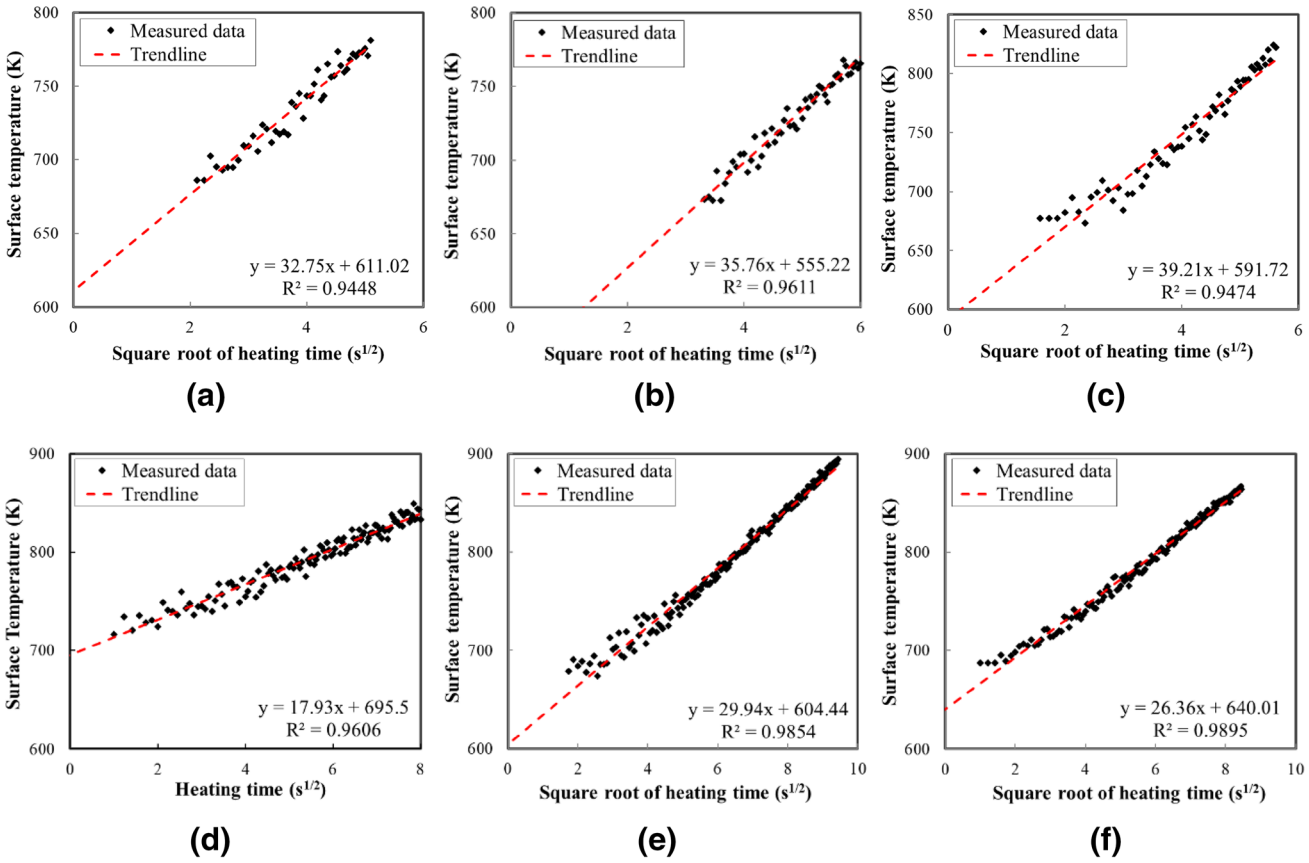

Fig. 6 Profile of surface temperatures with the change of heating time: **a** granite 1; **b** granite 2; **c** granite 3; **d** sandstone 1; **e** sandstone 2; **f** sandstone 3

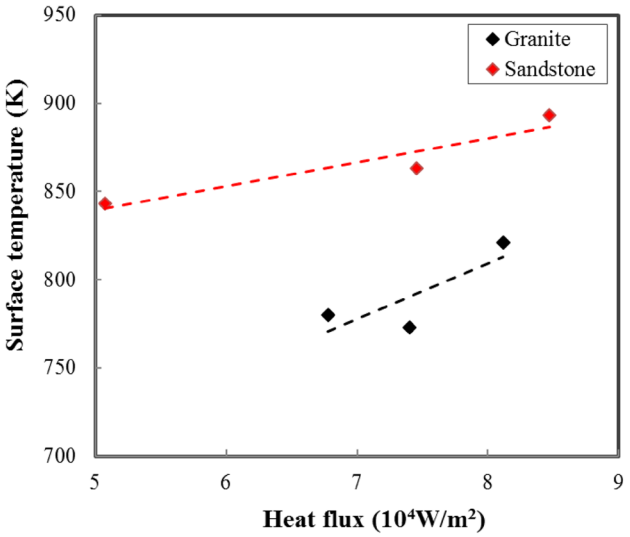

Fig. 7 Profile of surface temperatures with the change of heating flux: **a** granite 1; **b** granite 2; **c** granite 3; **d** sandstone 1; **e** sandstone 2; **f** sandstone 3

2016). First, the distance from the combustion chamber to the rock surface is large in our experiment. Second, the flame length in our experiment is short, meaning that a small heat flux acts on the rock surface. In addition, the heat flux should be designed for field applications. If the heat flux is too small, then the temperature of the rock surface will increase slowly, which may lead to an increase of the onset-spallation time and a decrease in the rate of penetration. If the heat flux is too large, then the temperature of the rock surface will increase too quickly, which may lead to rock melting and a decrease in the rate of penetration. This work presents specific cases about the heat flux and onset-spallation time. The average heat flux of the granite and sandstone samples are 7.43×10^4 and 7.00×10^4 W/m^2, respectively. Correspondingly, the average onset-spallation time of the granite and sandstone sample is 31.5 and 76.7 s, respectively.

4 Numerical Simulation Section

4.1 Model Description

A brief description of our model is presented here. First, we present the mathematical model. Second, we present the numerical model. The stress in the rock is obtained by

$$\sigma_{ij,j} + F_i = 0, \tag{3}$$

where $\sigma_{ij,j}$ is the stress tensor (Pa); and F_i represents body force (Pa). The geometrical equation can be expressed as

$$\varepsilon_{ij} = \frac{1}{2}(u_{i,j} + u_{j,i}), \tag{4}$$

where ε_{ij} is the strain tensor (dimensionless); and u represents displacement (m). Rock samples are assumed to be linear elastic materials. Hence, the constitutive equation can be expressed as

$$Gu_{i,jj} + \frac{G}{1-2\mu}u_{i,jj} - K'\alpha T_i + F_i = 0, \tag{5}$$

where G is the shear modulus (Pa); and K' is the rock expansion index (Pa), which can be obtained by

$$K' = \frac{2G(1+\mu)}{3(1-2\mu)}. \tag{6}$$

The temperature is obtained by solving the energy equation in the rock, which is obtained by

$$\rho C\frac{\partial T}{\partial t} = \nabla \cdot (K_r \nabla T), \tag{7}$$

where T is the temperature in the rock (K). It is important to mention that the effect of rock deformation on heat transfer is not considered in the paper. The maximum tensile stress criterion and Mohr–Coulomb criterion have been widely selected as the breakage thresholds in previous investigations (Zhu and Tang 2004; Zhu et al. 2014; Zhou et al. 2018). However, when the rock is heated by a high-temperature flame, plastic deformation may occur in the rock spallation process. Hence, in this paper, von Mises stress is used as the breakage threshold, and it can be expressed as

$$\sigma_v - \sigma_s \geqslant 0, \tag{8}$$

where σ_v is von Mises stress (N/m^2); and σ_s is the yield strength (N/m^2). The von Mises stress can be obtained by

$$\sigma_v = \sqrt{\frac{1}{2}[(\sigma_1-\sigma_2)^2 + (\sigma_2-\sigma_3)^2 + (\sigma_3-\sigma_1)^2]}, \tag{9}$$

where $\sigma_1, \sigma_2, \sigma_3$ are principal stresses (Pa). In this paper, the tensile stress is positive and the compressive stress is negative. The principal stresses are numbered conventionally in descending order of magnitude: $\sigma_1 > \sigma_2 > \sigma_3$.

A 3D numerical model is built as shown in Fig. 8. The model size is the same as the rock sample size (0.1×0.1×0.1 m), which is shown in Fig. 8a. A heating zone is assumed in the rock surface and has a diameter of 0.03 m (Fig. 8a). The heating zone equals the inner diameter of the combustion chamber. The thermal boundary conditions and force boundary conditions are shown in the longitudinal profiles along the centerline (Fig. 8b, c). The temperature in the heating zone is equal to the measured temperature by the infrared thermometer (B_1). The measured surface temperatures of all six specimens are shown in Fig. 9. Figure 9a–f represent the measured surface temperatures of granite 1, granite 2, granite 3, sandstone 1, sandstone 2, sandstone 3, respectively. The black dots in Fig. 9 are the measured surface temperatures of the rock specimens. The red dashed lines in Fig. 9 are tread lines obtained via the linear fitting, and they are used as the temperature boundary condition in the

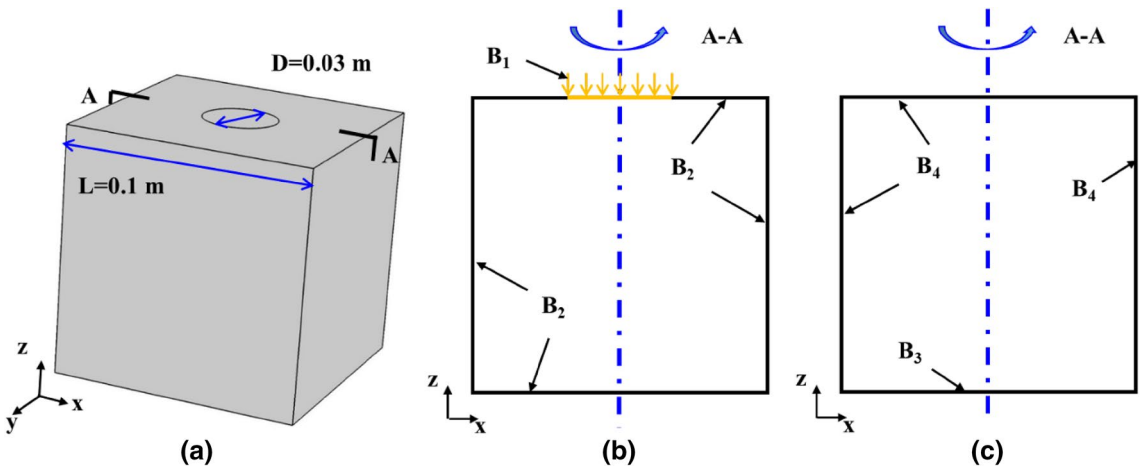

Fig. 8 The model size and boundary conditions **a** model size; **b** thermal boundary conditions; **c** force boundary conditions

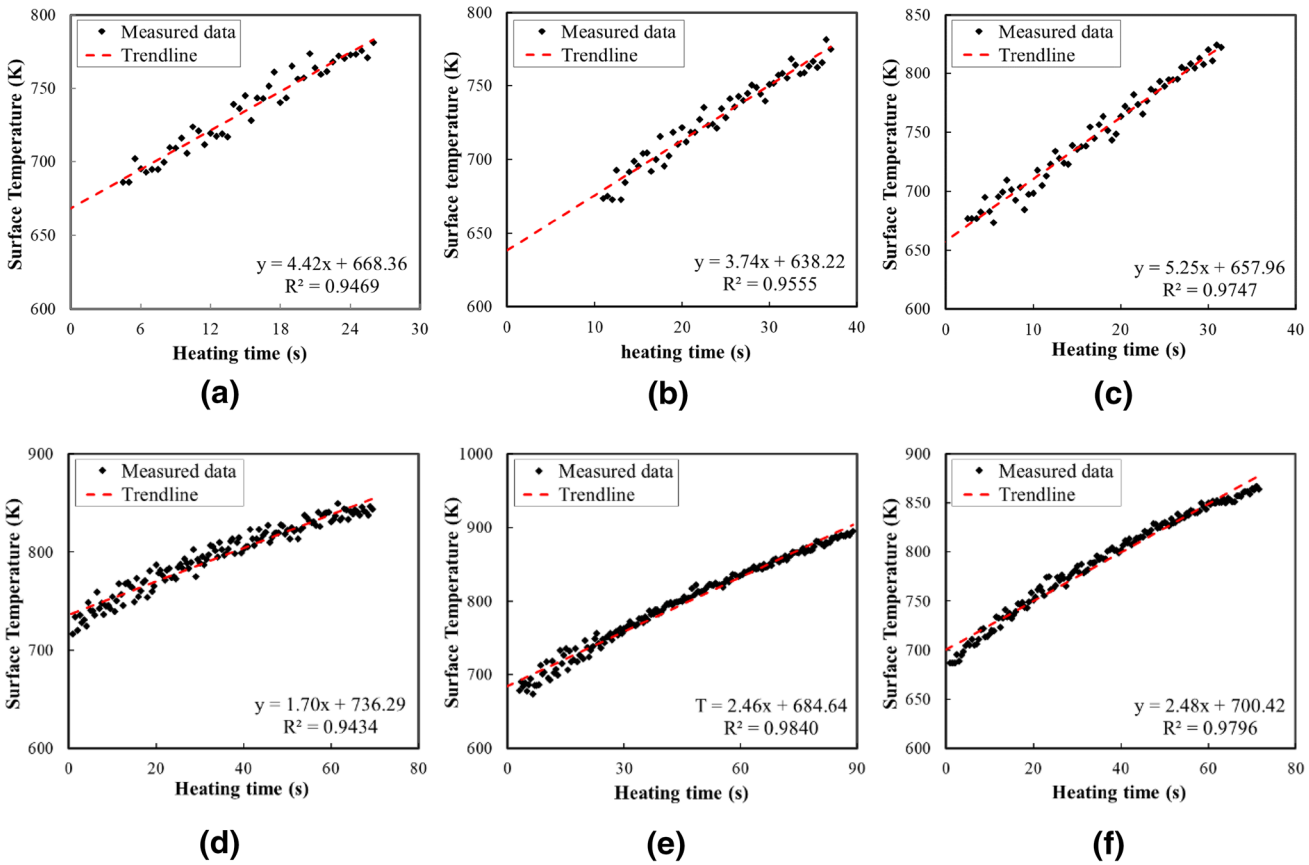

Fig. 9 The measured surface temperatures of granite and sandstone: **a** granite 1; **b** granite 2; **c** granite 3; **d** sandstone 1; **e** sandstone 2; **f** sandstone 3

heating zone (B_1) in the simulation. The temperature in the other zone (B_2) are controlled by convective heat flux; thus,

$$Q_0 = h_f \times (T_{ext} - T), \tag{10}$$

where Q_0 is the convective heat flux (W/m^2); T_b is the temperature on the boundary (K); h_f is the convective heat transfer coefficient [W/(m^2 K]; and T_{ext} is the ambient temperature, which is 280.15 K under our experimental conditions. Figure 8c presents the force boundary conditions of the model. The boundary condition of the rock bottom (B_3) is called roller, which means that the displacement in the Z direction is zero. The other boundaries (B_4) are set as free, which means that the boundaries (B_4) can deform freely. The material properties of granite and sandstone can be found in Table 2. The domain is discretized and solved in space using the finite element method. The Gauss integration method is implemented to evaluate all volume integrals in the weak form equations. All the equations are solved by a time-dependent solver. Specifically, physical models of solid mechanics and heat transfer in solid are used in the simulation. The rock is considered an isotropic linear elastic material. The initial displacement of the rock specimens is zero. The initial temperature in the internal of rock equals the ambient temperature under the experiment condition (280.15 K). A free triangular mesh is used at the top surface. The swept method is utilized to generate prism elements in the domain. The time step is 0.1 s. A physics-controlled method is used to calculate the tolerance.

The numerical model is validated via comparisons with the measured temperature in the rock. As shown in Fig. 4, the holes with a distance to the rock surface of 20 mm, 40 mm, 60 mm, and 80 mm are called hole 1, hole 2, hole 3, and hole 4, respectively. Since the rock samples have a low coefficient of thermal conductivity, the temperatures in hole 2, hole 3, and hole 4 change little as the heating time increases. We used the measured temperatures in hole 1 to validate our numerical model. The depth of the K thermocouple in hole 1 is 30, 20, 30, 17.5, 20, and 25 mm for granite 1, granite 2, granite 3, sandstone 1, sandstone 2, sandstone 3, respectively. A comparison of the measured temperature and simulated temperature is shown in Fig. 10. The *y*-axis in Fig. 10 is the difference between the surface temperature and the initial temperature ($t = 0$). The *x*-axis in Fig. 10 represents the heating times. In the validation section, the heating time is

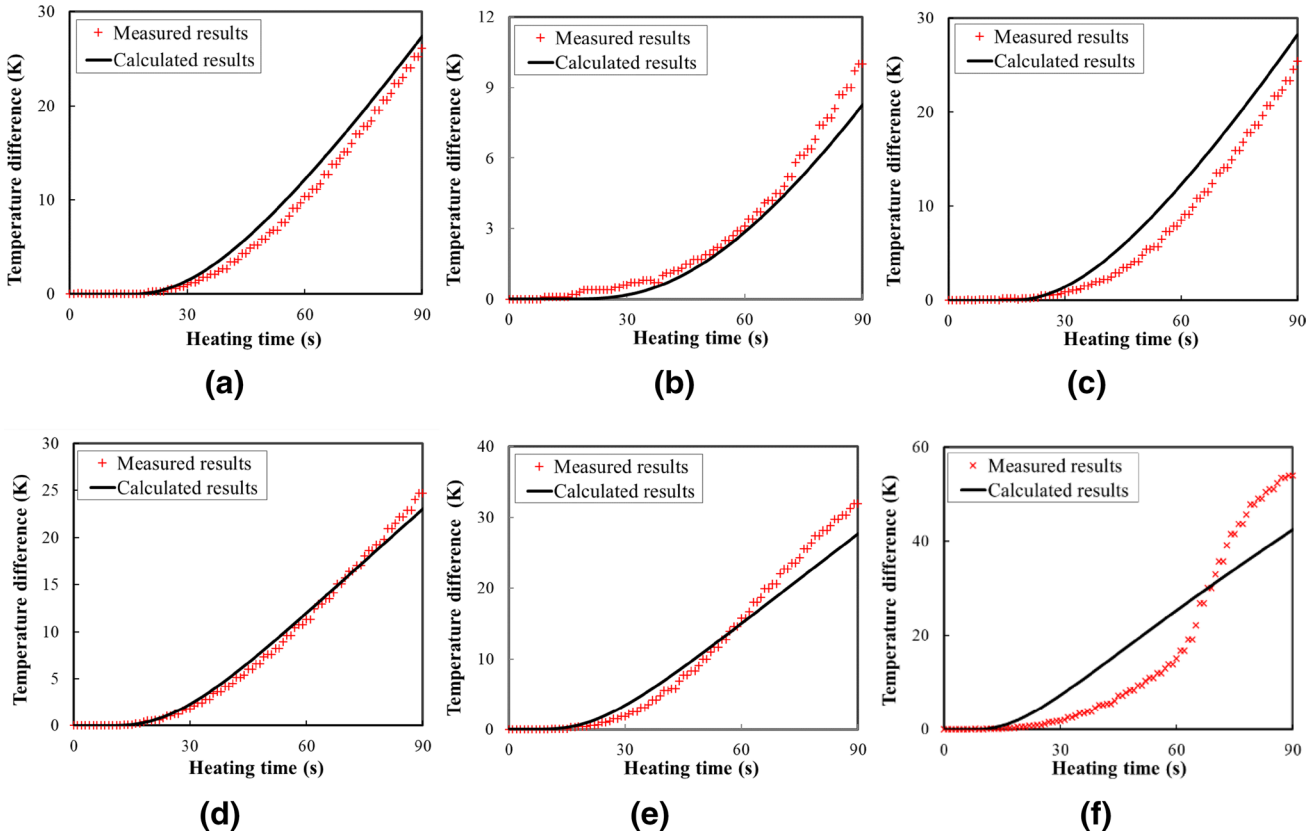

Fig. 10 Comparison between measured temperatures and simulated temperatures in hole 1: **a** granite 1; **b** granite 2; **c** granite 3; **d** sandstone 1; **e** sandstone 2; **f** sandstone 3

assumed to be 90 s, which is longer than the onset-spallation time of all specimens because the temperature increase in hole 1 is still minimal as the heating time increases. A longer heating time can provide a clear comparison between the simulation results and experimental results. The red markers and black full line in Fig. 10 represent the measured data and simulated data, respectively. As the heating time changes, the average errors between the simulated temperature and the measured temperature for granite 1, granite 2, and granite 3 are 6.95%, 4.28%, and 13.07%, respectively. The average error for all three granite specimens is 8.10%. Meanwhile, as the heating time changes, the average errors between the simulated temperature and the measured temperature for sandstone 1, sandstone 2, sandstone 3 are 2.77%, 7.99%, and 33.19%, respectively. The average error for all three granite specimens is 14.65%. An acceptable match can be obtained between the simulation results and measured results. The error of sandstone is higher than that of granite because more pores occur in sandstone than granite and additional micro-fractures can be induced in sandstone during the heating process. Pores and micro-fractures may affect the heat transfer in the interior of the sandstone, which is not considered in the simulation.

4.2 Temperature and Stress Distribution Comparisons

In this section, we select sandstone 2 and granite 2 to clarify the temperature and stress distribution in the rock. The temperature distribution in the vertical direction (X–Z profile) for granite 2 and sandstone 2 is shown in Fig. 11. The temperature distributions for granite with heating times of 10, 20, and 30 s, respectively, are shown in Fig. 11a–c. The temperature distributions for sandstone with heating times of 10, 20, 30 s, respectively, are shown in Fig. 11d–f. Only the temperature at the zone close to the rock surface presents a significant increase because the heat transfer in the rock is slow in both the granite and sandstone samples. The temperature at the zone far from the rock surface is almost unchangeable as the heating time increases. Compared with granite, sandstone has a larger high-temperature zone because of the larger coefficient of thermal conductivity. To obtain a quantitative understanding of the temperature distribution in granite and sandstone, we present the temperature along line L_1 and line L_2 with a heating time of 30 s as shown in Fig. 12. Line L_1 has a distance of 5 mm to the rock surface. Line L_2 is the centerline (Fig. 11). When the X coordinate

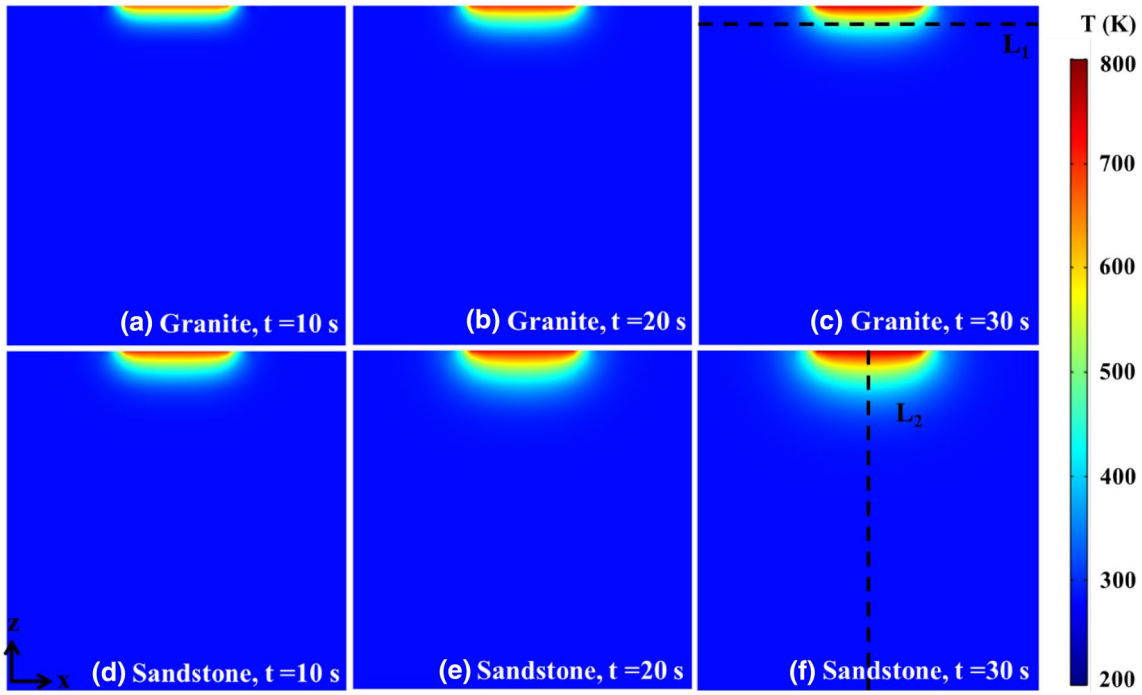

Fig. 11 Comparison of temperature distribution at the vertical direction for granite and sandstone. The heating time is 10, 20, 30 s, respectively

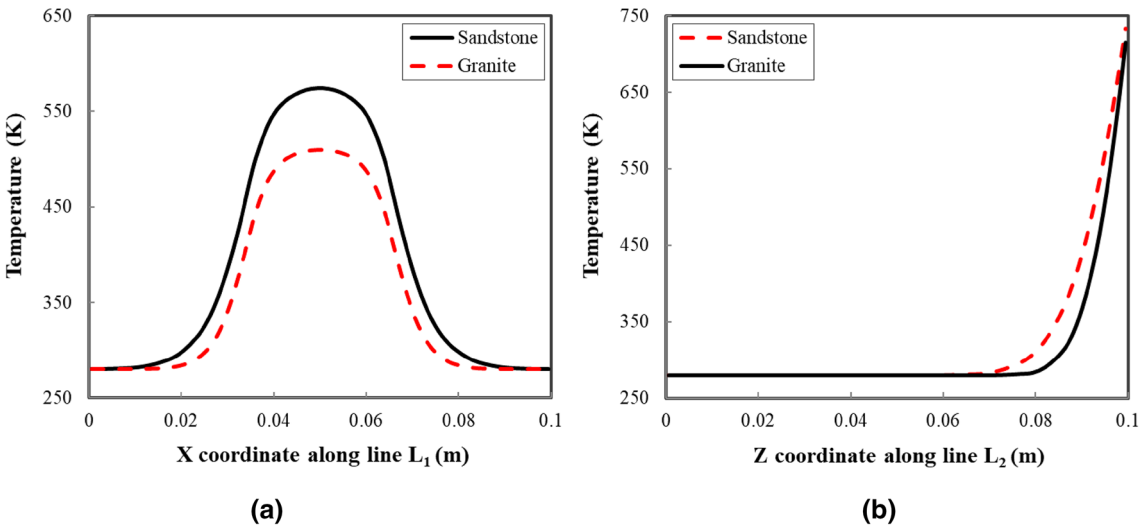

Fig. 12 Profiles of temperature distribution along line L_1 and L_2: **a** profile of temperature distribution along line L_1; **b** profile of temperature distribution along line L_2

at line L_1 is 0.05 m, the temperature of sandstone 2 is higher than that of granite 2 by 12.58%. When the Z coordinate at line L_2 is 0.09 m, the temperature of sandstone 2 is higher than that of granite 2 by 18.90%.

The stress distribution in the granite and sandstone samples is compared in this section. The von Mises stress in the vertical direction (X–Z profile) for granite 2 and sandstone 2 is shown in Fig. 13, and it is used to compare the equivalent stress in granite and sandstone. Higher von Mises stresses are induced in the granite sample than the sandstone sample (Fig. 13). We present the von Mises stress along line L_3 and line L_4 with a heating time of 30 s as shown in Fig. 14. Line L_3 has a distance of 5 mm to the rock surface. Line L_4 is the centerline (Fig. 13). When the x coordinate at line L_3 is 0.05 m, the von Mises stress of granite 2 is higher than that of sandstone 2 by 13.77% (Fig. 14a). When the Z coordinate

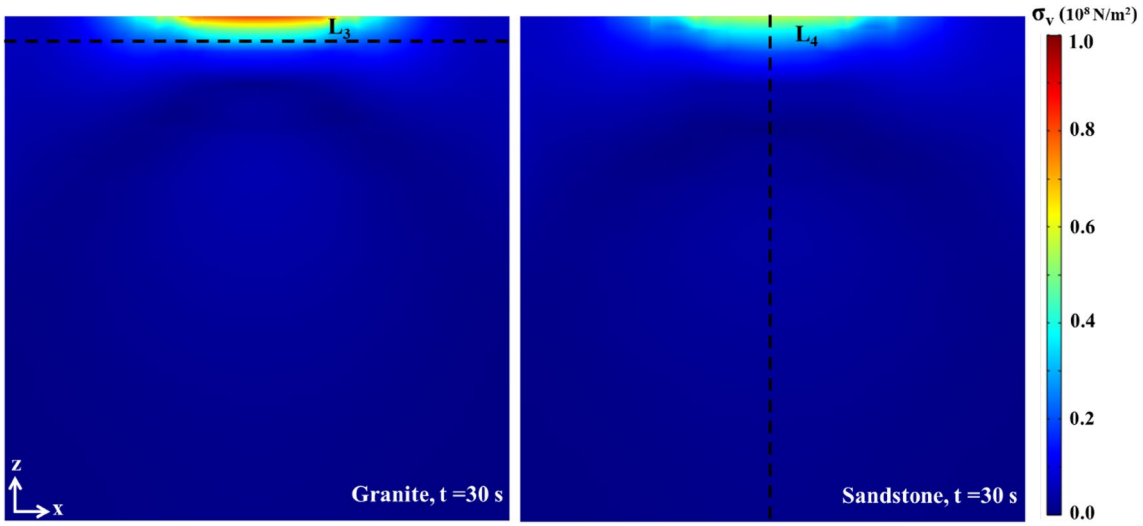

Fig. 13 The von Mises stress of granite and sandstone when the heating time is 30 s

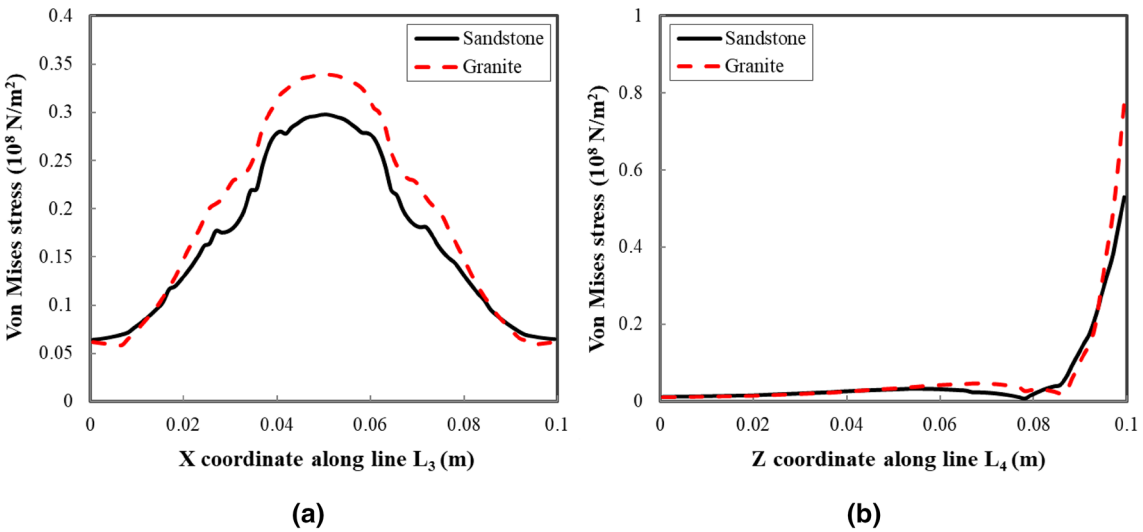

Fig. 14 Profiles of von Mises stress along line L_3 and L_4: **a** profile of von Mises stress along line L_3; **b** profile of von Mises stress along line L_4

at line L_4 is 0.1 m, the von Mises stress of granite 2 is higher than that of sandstone 2 by 46.74% (Fig. 14b). Since the equivalent stress (von Mises stress) of the granite samples is larger than that of the sandstone samples, spalls are more easily generated in the granite sample than the sandstone sample, which is consistent with the experimental result.

4.3 Comparison of the Breakage-Probability Index

In this section, the breakage-probability index is used to compare the simulated results and experimental results. In the experiment section, the onset-spallation time at which the first spall is generated at the rock surface is obtained. Here, the stress distribution in the rock is simulated using a heating time equal to the onset-spallation time. After that, a breakage-probability factor is defined to represent the possibility of rock breakage. If the breakage-probability factor is larger, then the rock has a higher likelihood of being broken. A breakage-probability factor equal to 1 in the simulation means the rock is broken, and it roughly corresponds to the generation of the first spall at the rock surface in our experiment. In this paper, the breakage-probability factor is defined by the ratio of von Mises stress and yield strength, which can be expressed as

$$f_b = \frac{\sigma_v}{\sigma_s}, \tag{12}$$

where f_b is the breakage-probability factor (dimensionless).

First, we compared the simulated results and experimental results. The breakage-probability factor of granite 2 and sandstone 2 in the vertical direction (X–Z profile) is shown in Fig. 15. The heating times for granite and sandstone is 37 and 89 s, which equals the onset-spallation time of granite 2 and sandstone 2, respectively. As presented in Fig. 15, the high breakage-probability zones occur near the rock surface for both granite and sandstone, which is consistent with the experimental results. The first spall is generated inside the zone where the rock surface is heated directly. The comparison between the experimental and simulation results is shown in Fig. 16. When the heating time equals the onset-spallation time, the first spall can be observed in the granite and sandstone experiments. Hence, the breakage-probability factor should equal 1 for the experimental results. Correspondingly, when the heating time equals onset-spallation time, the largest breakage-probability factors of granite and sandstone at the surface are 0.91 and 0.82, respectively, which means that granite and sandstone have a high possibility of breakage. Meanwhile, we can infer that with the von Mises criterion, the simulation results can provide acceptable predictions of the onset of granite breakage. However, we have to mention that the simulation still slightly underestimates the possibility of granite and sandstone breakage. The error between the simulation results and the experimental results is mainly caused by the model assumptions. Heterogeneity, micro-flaws, and plasticity are not considered in the simulation, which may affect the possibility of rock breakage. First, the increase of heterogeneity may enhance the possibility of rock breakage. Second, pore and micro-flaws in the rock may become expanded and connected when the rock surface is heated and thus may also enhance the possibility of rock breakage. Third, the plasticity of rock may increase as the heating time increases, which may reduce the possibility of rock breakage.

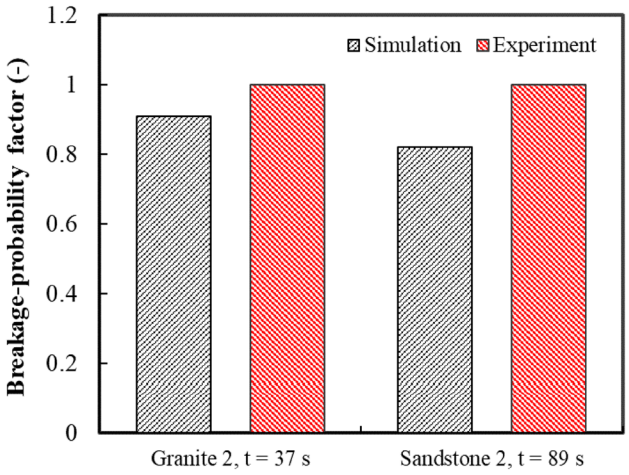

Fig. 16 The comparison between experiment and simulation for granite 2 and sandstone 2

Second, we compared the breakage-probability factor of granite 2 and sandstone 2 in the vertical direction (X–Z profile) with the same heating time of 37 s (Figs. 17, 18). The heating time equals the measured onset-spallation time of granite 2. Compared to sandstone 2, when the heating time is the same, granite 2 has a higher possibility of breaking because the breakage-probability factor of granite is higher than that of sandstone at the rock surface in the heating zone (Fig. 17). This finding is consistent with the experimental results. The onset-spallation time of granite 2 is lower than that of sandstone 2. To obtain

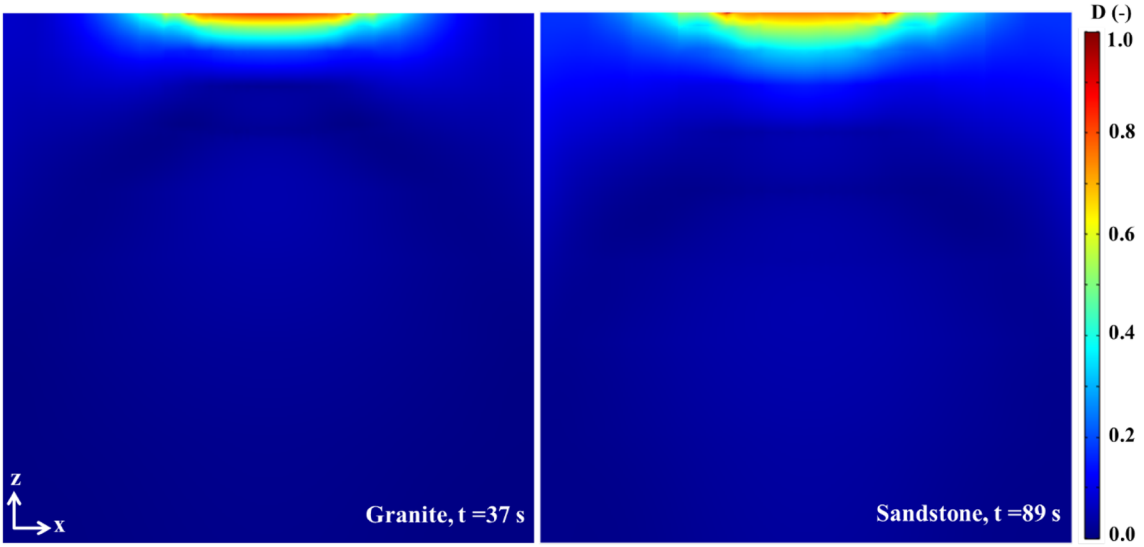

Fig. 15 The breakage-probability factor of granite 2 and sandstone 2. The heating times of granite sandstone are 37 and 89 s, respectively

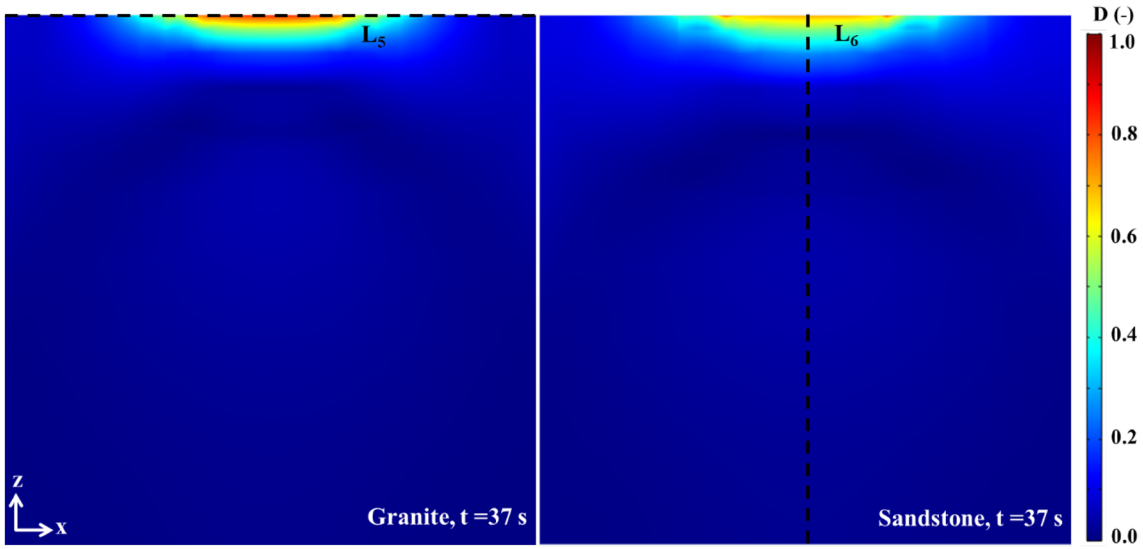

Fig. 17 The breakage-probability factor of granite and sandstone when the heating time is 37 s

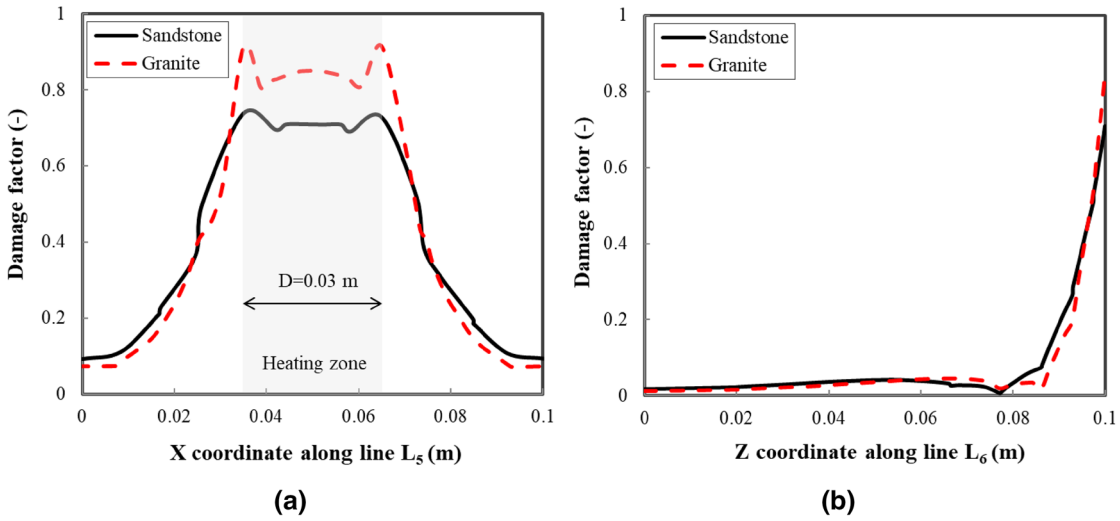

Fig. 18 Profiles of breakage-probability factor line L_5 and L_6: **a** profile of breakage-probability factor line L_5; **b** profile of breakage-probability factor along line L_6

a quantitative understanding of the breakage-probability factor of granite and sandstone, we present the breakage-probability factor along lines L_5 and L_6 as shown in Fig. 18. Line L_5 is at the rock surface, and line L_6 is at the center line. A comparison of the breakage-probability factors of granite samples and sandstone samples along line L_5 is shown in Fig. 18a. The heating zone at the rock surface indicates the zone that is heated with a high temperature. The breakage-probability factor of granite 2 is higher than that of sandstone 2 in the heating zone. When the x coordinate equals 0.05, the breakage-probability factor of granite 2 is larger than that of sandstone 2 by 19.69%. The breakage-probability factor of granite 2 and sandstone 2 is approximately the same outside of the heating zone. A comparison of the breakage-probability factors of granite 2 and sandstone 2 along line L_6 is shown in Fig. 18b. When the distance to the rock surface is less than 3 mm, the breakage-probability factor of granite 2 is higher than that of sandstone 2. When the distance to the rock surface is larger than 14 mm, the breakage-probability factor of granite 2 and sandstone 2 are minimal (less than 0.1). Thus, we can conclude that rock breakage occurred near the rock surface for both sandstone 2 and granite 2.

5 Conclusions

In this study, experiments and simulations were performed to investigate the lowest required surface temperature in thermal spallation for one type of granite and sandstone. First, we conduct a thermal spallation experiment for the granite and sandstone samples. The lowest required surface temperature of the granite and sandstone samples is measured by an infrared thermometer. Then, the heat flux is evaluated and compared between the sandstone and granite samples. Meanwhile, a three-dimensional numerical model is built to simulate the heat transfer and stress distribution in the rock samples. The temperature and von Mises stress are compared in the sandstone and granite samples, and then the breakage-probability factor of the tested granite and sandstone samples are compared. The following conclusions are obtained by this study:

1. Under our experimental conditions, the average lowest required surface temperature in the sandstone samples is slightly higher than that of the granite samples. The average LRSTs for the granite and sandstone samples are 791.48 K and 842.40 K, respectively.
2. Under our experimental conditions, the onset-spallation time of the sandstone samples is longer than that of the granite samples. The average onset-spallation time of the granite and sandstone samples is 31.50 s and 65.75 s, respectively.
3. Only the temperature at the zone closed to the rock surface presents a significant increase for both granite and sandstone. The temperature at the zone far from the rock surface is almost unchangeable as the heating time increases.
4. When the heating time is equivalent, the von Mises stresses near the surface of the granite samples are higher than that of the sandstone samples. Meanwhile, a higher breakage-probability factor can be achieved near the surface of the granite samples than the sandstone samples.

The limitations of our work are discussed here. First, we are focused on investigating the LRST for one type of granite and sandstone. Thus, careful consideration must be exercised when using our conclusions for different granites and sandstones. Additional efforts should be focused on investigating the LRST in more types of granite and sandstone specimens. Second, in this paper, we only tested three specimens for granite and sandstone. Hence, the relationship between the heat flux and surface temperature should be further investigated in future studies. Third, the heterogeneity, micro-flaws, and plasticity are not considered in our model. A more complex model should be developed in future work to accurately simulate the process of rock breakage.

Acknowledgements The authors would like to acknowledge the financial support from the National Natural Science Foundation of China (no. U1562212 and no. 51504272) and National Key Research and Development Program of China (2016YFE0124600).

References

Augustine CR (2009) Hydrothermal spallation drilling and advanced energy conversion technologies for engineered geothermal systems, Ph.D. thesis, Massachusetts Institute of Technology, Massachusetts

Beentjes I, Bender JT, Hillson SD.,Tester JW (2018) Hydrothermal spallation of barre granite using supercritical water jets. Proceedings, 43rd workshop on Geothermal Reservoir Engineering Stanford University, Stanford, California

Brkic D, Kant M, Meier T, Schuler MJ, Rohr R (2015) Influence of process parameters on thermal rock fracturing under ambient conditions. Proceedings World Geothermal Congress 2015. Melbourne, Australia

Carslaw HS, Jaeger JC (1959) Conduction of heat in solids. Oxford University Press, Oxford

Dey TN (1984) More on spallation theory. In: Los Alamos National Laboratory Internal Memorandum No. E55-3-286-84

Dey TN, Kranz RL (1987) Flake mechanics, borehole breakouts, and thermal spallation. In: Proceedings of the 28th US symposium on rock mechanics, Tucson, Arizona

Hettema M, Wolf KH, Pater CD (1998) The influence of steam pressure on thermal spalling of sedimentary rock: theory and experiments. Int J Rock Mech Min Sci 35(1):3–15

Hu X, Song X, Li G, Shen Z, Cui L, Lv Z, Shi Y (2016) Numerical analysis of bottomhole velocity and pressure distributions of high pressure high temperature hydrothermal jet. In: SPE/IADC Asia Pacific Drilling Technology Conference, Singapore

Hu X, Song X, Li G, Shen Z, Lyu Z, Shi Y (2018a) Shape factor of the flake-like particle in thermal spallation and its effects on settling and transport behavior in drilling annulus. Powder Technol 335:211–221

Hu X, Song X, Li G, Shen Z, Lyu Z, Shi Y, Zheng R (2018b) An analytical model to evaluate the heating conditions for drilling in hard rock using an innovative hydrothermal spallation method. Appl Therm Eng 142:709–716

Kant MA, von Rohr PR (2016) Minimal required boundary conditions for the thermal spallation process of granitic rocks. Int J Rock Mech Min Sci 84:177–186

Lyu Z, Song X, Shi Y, Li G, Hu X, Zheng R, Wang G (2017) Analysis on feasibility of rock thermal spallation drilling utilizing specific energy method. American Rock Mechanics Association, San Francisco

Potter RM, Potter JM, Wideman TW (2010) Laboratory study and field demonstration of hydrothermal spallation drilling. GRC Trans 34:249–252

Preston FW, White HE (1934) Observations on spalling. J Am Ceram Soc 17:137–144

Rauenzahn RM (1986) Analysis of rock mechanics and gas dynamics of flame-jet thermal spallation drilling. Ph.D. thesis, Massachusetts Institute of Technology, Massachusetts

Rauenzahn R, Tester J (1989) Rock failure mechanisms of flame-jet thermal spallation drilling-theory and experimental testing. Int J Rock Mech Min Sci Geomech Abst 26(5):381–399

Rauenzahn RM, Tester JW (1991a) Numerical simulation and field testing of flame-jet thermal spallation drilling-1. Model development. Int J Heat Mass Trans 34(3):795–808

Rauenzahn RM, Tester JW (1991b) Numerical simulation and field testing of flame-jet thermal spallation drilling-2. Experimental verification. Int J Heat Mass Trans 34(3):809–818

Rothenfluh T (2013) Heat transfer phenomena of supercritical water jets in hydrothermal spallation drilling, Ph.D. thesis, Swiss Federal Institute of Technology, Zurich

Rothenfluh T, Schuler MJ, Rohr PR (2011) Penetration length studies of supercritical water jets submerged in a subcritical water environment using a novel optical Schlieren method. J Supercrit Fluids 57:175–182

Sierra-Pallares J, Parra-Santos MT, García-Serna J, Castro F, Cocero MJ (2009) Numerical modeling of hydrothermal flames. Micromixing effects over turbulent reaction rates. J Supercrit Fluids 50(2):146–154

Song X, Lv Z, Li G, Hu X, Shi Y (2017) Numerical analysis on the impact of the flow field of hydrothermal jet drilling for geothermal wells in a confined cooling environment. Geothermics 66:39–49

Stacey RW, Sanyal S, Potter J, Wideman T (2011) Effectiveness of selective borehole enlargement to improve flow performance of geothermal wells. GRC Trans 35:239–245

Walsh SDC (2013) Modeling thermally induced failure of brittle geomaterials. Technical Report No. LLNL-TR-632239, Lawrence Livermore National Laboratory (LLNL), Livermore, CA

Walsh SDC, Lomov IN (2013) Micromechanical modeling of thermal spallation in granitic rock. Int J Heat Mass Trans 65:366–373

Walsh SDC, Lomov I, Roberts JJ (2011) Geomechanical modeling for thermal spallation drilling. LLNL-PROC-483098. In: Geothermal Resources Council 35th Annual Meeting, San Diego, CA, United States

Walsh SDC, Lomov IIya N, Wideman TW, Potter JM (2014) Size-dependent spall aspect ratio and its effects in thermal spallation. Int J Rock Mech Min Sci 70:375–380

Wilkinson MA, Tester JW (1993) Experimental measurement of surface temperatures during flame-jet induced thermal spallation. Rock Mech Rock Eng 26(1):29–62

Williams RE, Potter RM, Miska S (1996) Experiments in thermal spallation of various rocks. Transactions of the ASME 118:2–8

Zhou J, Wei J, Yang T, Zhu W, Li L, Zhang P (2018) Damage analysis of rock mass coupling joints, water and microseismicity. Tunn Undergr Sp Tech 71:366–381

Zhu W, Tang C (2004) Micromechanical model for simulating the fracture process of rock. Rock Mech Rock Eng 37(1):25–56

Zhu W, Wei J, Zhao J, Niu L (2014) 2D numerical simulation on excavation damaged zone induced by dynamic stress redistribution. Tunn Undergr Sp Tech 43:315–326